Mechanics-Based Modeling Approach for Rapid Prediction of Low Velocity Impact Damage in Composite Laminates

Luke B. Borkowski,[1] and Rajesh S. Kumar[2]
United Technologies Research Center, East Hartford, CT, 06108, USA

Upul R. Palliyaguru[3]
National Institute for Aviation Research - Wichita State University, Wichita, KS, 67260, USA

A mechanics-based modeling approach is developed to rapidly predict damage in polymer matrix composites resulting from a low velocity impact event. The approach is incorporated into a computer code that provides an efficient means to assess the damage resistance for a range of material systems, layup configurations, and impact scenarios. It is envisioned that the developed approach will aid in early design and analysis of composite structures where sizing and layup decisions must be made, and evaluating the feasibility of a large number of laminate configurations using numerical approaches such as finite element analysis (FEA) is prohibitively expensive. Therefore, the goal of the modeling approach is to predict the impact damage size given the laminate configuration and impact scenario. This information can then be used to determine the residual strength of the material. To be useful in such a context, the tool is designed to run quickly (<2 minutes) to allow a large number of design cases to be investigated. The results presented demonstrate that the model is capable of efficiently predicting low velocity impact damage size, shape, and location within an acceptable accuracy suitable for preliminary design and analysis of composite structures.

[1] Staff Research Engineer, Physical Sciences Department
[2] Associate Research Director, Physical Sciences Department
[3] Sr. Research Engineer, National Institute for Aviation Research – Wichita State University

I. Introduction

Impact resistance and subsequent reduction in residual strength are key properties needed for initial sizing and design of aerospace composite structures. Compression after impact (CAI) strength is of particular interest because of the significant reduction in compression strength due to impact – up to 60% [Maio et al., 2013]. Typically these properties are measured experimentally for each laminate configuration under consideration for design. Because of the large number of parameters defining the material such as laminate configuration (e.g., layup, ply thickness, and fiber architecture) and impact scenario (e.g., impactor radius, mass, and energy or velocity), performing tests for every possible combination is intractable (i.e., time consuming and prohibitively expensive). Therefore a small subset of combinations, typically based on past design experience, are tested and the results used for developing design allowables and/or design optimization. This approach inherently limits the design space and may result in sub-optimal design choices early in the design process and/or incorrect design decisions that can lead to expensive redesigns later on in the process.

In order to mitigate the large expense of creating new data for composite laminate design optimization, a modeling framework for the prediction of barely visible impact damage (BVID) and CAI strength has been developed. It should be noted that, in this paper, the terms BVID and low velocity impact are used interchangeably to describe an impact event that results in predominantly sub-surface damage in the composite without significant surface damage or perforation. The modeling framework can serve effectively as a rapid design tool since it is based on closed-form analytical and semi-analytical methods requiring minimal user pre-processing and short computational run time. Details of the previously-developed rapid CAI strength model can be found in Refs. [Borkowski and Kumar, 2018a; Borkowski and Kumar, 2018b] which describe a model that takes as input impact damage information from an experiment or model and provides the CAI strength as output. The BVID model presented here is designed to couple with the rapid CAI model [Borkowski and Kumar, 2018a; Borkowski and Kumar, 2018b] in order to yield a comprehensive, mechanics-based rapid BVID/CAI strength prediction modeling framework.

Predicting impact damage in composite plates involves first resolving the plate transient deformation/kinematics as a result of the impact event and then determining the resulting damage. Given the efficiency requirements of a rapid design and analysis tool, the form of the plate kinematic and damage prediction models must be chosen carefully. Extensive research has been conducted on the development of composite impact models. While a comprehensive overview of the field [Abrate, 2005] is beyond the scope of the current paper, a few works relevant to the developed

model will be described. These works focus on mechanics-based methods, typically solved analytically or semi-analytically, which can run in a few minutes or less compared to finite element analysis (FEA) based models that require longer runtimes on the order of hours. The problem of impact on a composite plate has been investigated by Sun and Chattopadhyay [1975], Dobyns [1981], Cairns and Lagace [1989], and Qian and Swanson [1990]. For composite plates, [Whitney and Pagano, 1970] demonstrated the significant contribution of shear deformation due to the high transverse shear compliance. Therefore in analyzing impact on composite laminates, the first-order shear deformation theory (FSDT) is recommended to avoid unrealistically stiff solutions. Dobyns [1981] expanded on the approach by Sun and Chattopadhyay [1975], which considered impact on a simply supported orthotropic Mindlin-Reissner plate [Whitney and Pagano, 1970] with a point load, by replacing the concentrated impact load with uniform patch pressure to avoid the transverse shear stress singularity at the contact point. Since both Sun and Chattopadhyay [1975] and Dobyns [1981] analyzed simply supported plates, they were able to employ the Navier solution to simplify the governing equations of motion and achieve an exact solution. In order to employ more general boundary conditions, Cairns and Lagace [1989] and Qian and Swanson [1990] utilized the Rayleigh-Ritz variational method, along with appropriate assumed mode shapes which satisfy the essential boundary conditions, to solve for composite plate response under impact loading.

While these methods have been shown capable of predicting the response of a composite plate to impact, few methods are also able to accurately simulate the resulting damage. A maximum transverse shear stress-based approach was employed by Dobyns [Dobyns, 1981] to estimate the size of delamination due to impact. In this approach, a scaled composite interlaminar shear strength is used in conjunction with the maximum interlaminar shear stress to predict the delamination size. Dobyns and other researchers (for example, [Dobyns, 1981; Chang and Chang, 1987; Brewer and Lagace, 1988]) have suggested that the scale factor can be treated as a material parameter, and is presumably, independent of laminate configuration or layup. However in preliminary investigations by the present authors, it was found that the stress-based scaling parameter is layup-dependent, and hence, is not suitable for design evaluation where multiple laminate configurations must be analyzed. In order to overcome this limitation, the present work uses a fracture-based approach for damage prediction, as discussed in Section IIB. Since the goal of the developed modeling framework is to rapidly predict impact damage and residual strength, an impact model capable of not only predicting plate transient response but also damage is desired. Therefore, components of various models from impact to composite damage are adapted to yield a comprehensive rapid BVID prediction model.

The paper is organized as follows: in Section II we present the BVID model in two parts: 1) Plate model for transient response to impact presented in Section IIA and 2) Details of the impact damage model provided in Section IIB. In Section III we present the experimental setup and demonstrate the model's ability to accurately predict impact damage over a wide range of laminates and impact parameters. Concluding remarks are presented in Section IV.

II. Low Velocity Impact Damage Model

The impact model consists of two sequentially coupled steps. In the first step, the transient response of the composite laminate is calculated using plate kinematics coupled with the impactor motion via Hertzian contact interaction. In the second step, the stress field obtained from the first step is used to calculate the resulting damage. The model was designed to be as general as possible while still maintaining the requisite computational efficiency to serve as a rapid analysis tool. Since, to the authors' knowledge, no model currently exists that satisfied all the features desired for a general, computationally efficient impact damage prediction tool, various components of individual models from existing literature were adapted into a framework that would satisfy this goal. In addition, enhancements were made to the component models for compatibility, improved accuracy, and greater generality. The salient features of the composite impact damage model for BVID prediction include:

1. The deformation of the composite plate is governed by Mindlin-Reissner first-order shear deformation theory [Reissner, 1945; Mindlin, 1951; Whitney and Pagano, 1970].
2. The solution to the transient impact problem is based on Lagrange's equation of motion where the Rayleigh-Ritz method is used to discretize the solution space.
3. This technique permits general application to plates with a wide range of boundary conditions and loads. In addition, the area of impact is finite and its location is arbitrary. This feature allows the model to simulate an impact event anywhere on the plate while the impact force is distributed over a finite area, thereby resulting in physically reasonable stresses under and near the impactor, which is crucial for predicting damage based on these stresses.
4. Coupling between the impactor and the transient behavior of the plate is achieved through the Hertzian contact law. This results in a series of coupled equations where the plate vibration is driven by the force exerted on the plate by the impactor.
5. The resulting impact-induced delamination state is computed using a fracture-based approach. In this approach, the strain energy (due to bending and transverse shear) stored in the laminate and released due

to the initiation and propagation of damage is calculated and compared with the critical strain energy release rate to determine the location, shape, and size of delamination.

A. Composite Plate Deformation Model

The formulation for the transient impact deformation model presented here is adapted from Refs. [Dobyns and Porter, 1981; Cairns and Lagace, 1989; Qian and Swanson, 1990]. The impact analysis of the composite plate, assuming its global deformation is independent of the local impactor contact deformation details, is based on Lagrange's equation of motion for conservative systems,

$$\frac{d}{dt}\frac{\partial L}{\partial \dot{\boldsymbol{x}}} - \frac{\partial L}{\partial \boldsymbol{x}} = 0 \tag{1}$$

where $\boldsymbol{x}$ is the generalized coordinates/modal amplitude, $\dot{\boldsymbol{x}}$ is the time derivative of the generalized coordinates/modal amplitude, and the Lagrangian function, L, is expressed as

$$L = KE - PE \tag{2}$$

where KE is the plate kinetic energy and PE is the potential energy. Assuming that the in-plane and rotary inertia effects are negligible, as suggested by Refs. [Birman and Bert, 1987; Dobyns, 1981, Cairns and Lagace, 1989; Qian and Swanson, 1990], the kinetic energy of the plate can be expressed as a function of the plate lateral velocity ($\dot{w}(x,y,t)$) as:

$$KE = \frac{\rho h}{2}\iint_{A_p} \dot{w}(x,y,t)^2 dA_p \tag{3}$$

where ρ is the plate mass density, h is the plate thickness, and the overdot indicates a derivative with respect to time. The potential energy for an anisotropic Mindlin-Reissner plate, neglecting membrane effects, includes the energy contributions from bending, transverse shear, and the work done by lateral impact loading [Whitney and Pagano, 1970; Qian and Swanson, 1990]. The normal transverse and membrane deformation of the plate are assumed negligible and therefore not included in the potential energy. The resulting expression for the potential energy is:

$$
\begin{aligned}
PE = \frac{1}{2}\iint_{A_p}\Bigg\{ & D_{11}\left(\frac{\partial \phi_x}{\partial x}\right)^2 + 2D_{12}\left(\frac{\partial \phi_x}{\partial x}\right)\left(\frac{\partial \phi_y}{\partial y}\right) + 2D_{16}\left(\frac{\partial \phi_x}{\partial x}\right)\left(\frac{\partial \phi_y}{\partial x}+\frac{\partial \phi_x}{\partial y}\right) \\
& + D_{22}\left(\frac{\partial \phi_y}{\partial y}\right)^2 + 2D_{26}\left(\frac{\partial \phi_y}{\partial y}\right)\left(\frac{\partial \phi_y}{\partial x}+\frac{\partial \phi_x}{\partial y}\right) + D_{66}\left(\frac{\partial \phi_y}{\partial x}+\frac{\partial \phi_x}{\partial y}\right)^2\Bigg\} dA_p \\
& + \frac{k}{2}\iint_{A_p}\Bigg\{ A_{44}\left(\phi_y+\frac{\partial w}{\partial y}\right)^2 + 2A_{45}\left(\phi_y+\frac{\partial w}{\partial y}\right)\left(\phi_x+\frac{\partial w}{\partial x}\right) + A_{55}\left(\phi_x+\frac{\partial w}{\partial x}\right)^2\Bigg\} dA_p \\
& - \iint_{A_c} q(x,y,t)w(x,y,t)dA_c
\end{aligned}
\tag{4}
$$

where

$$
\iint_{A_p} dA_p = \int_0^{L_y}\int_0^{L_x} dxdy \tag{5}
$$

is a surface integral taken over the entire plate and

$$
\iint_{A_c} dA_c = \int_{\eta-\frac{\sqrt{A_c}}{2}}^{\eta+\frac{\sqrt{A_c}}{2}}\int_{\xi-\frac{\sqrt{A_c}}{2}}^{\xi+\frac{\sqrt{A_c}}{2}} dxdy \tag{6}
$$

is a surface integral over the contact area. Here L_x and L_y are the dimensions of the plate in the x and y directions, respectively, ξ and η are the locations of the impact in the x and y directions, respectively, A_p is the plate area, A_c is the time-dependent contact area, and $\xi,\eta > \sqrt{A_c}/2$. Fig. 1 provides a schematic of the plate with the impact location parameters highlighted. Additionally in Eq. (4), the components of D and A are the plate bending and transverse shear stiffnesses, respectively, k is the shearing correction factor commonly used in FSDT [Mindlin, 1951], and $q(x,y,t)$ is the lateral load on the plate. For the shearing correction factor, a value of 5/6 is prescribed based on previous studies demonstrating its adequacy for laminates comprising thin plies [Whitney and Pagano, 1970]. Note in the expression for PE the presence of D_{16} and D_{26} indicating that the bend-twist coupling of the plate is considered in the analysis. Due to the requisite orthogonality of the modal shape functions (X_m and Y_n), the lateral load can be expressed as

$$
q(x,y,t) = \sum_m \sum_n Q_{mn}(t) X_m(x) Y_n(y) \tag{7}
$$

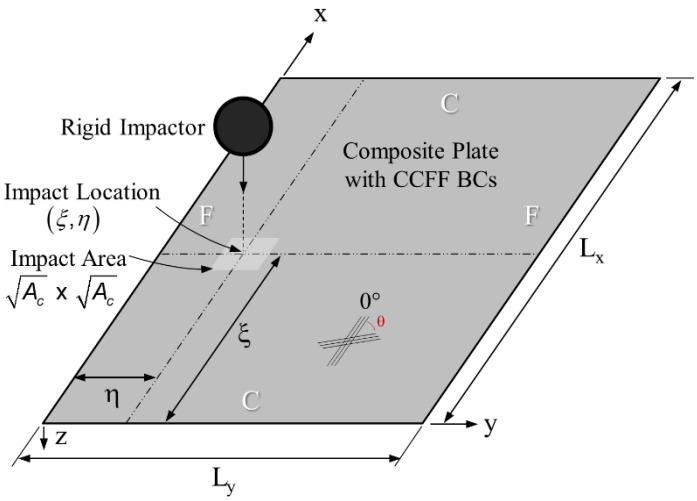

Fig. 1 Plate impact parameter illustration

In order to discretize Lagrange's equation of motion, the plate field variables (displacement and rotations) are approximated in discrete form. The series approximations for the transverse displacement (w) and planar rotations (ϕ_x and ϕ_y) are presented in Eqs. (8), (9), and (10). In these equations, the field variables are represented as the sum of the product of modal amplitudes (W_{mn} , A_{mn} , and B_{mn}), which are only functions of time, and assumed mode shape functions (X_m and Y_n), which are only functions of location and are assumed spatially separable. The prime on the assumed mode shape functions represents a derivative with respect to the independent spatial variable. The modal shape functions are chosen to satisfy the boundary conditions whereas the modal amplitudes must be determined through the solution methodology.

$$w(x,y,t) = \sum_m \sum_n W_{mn}(t) X_m(x) Y_n(y) \tag{8}$$

$$\phi_x(x,y,t) = \sum_m \sum_n A_{mn}(t) X'_m(x) Y_n(y) \tag{9}$$

$$\phi_y(x,y,t) = \sum_m \sum_n B_{mn}(t) X_m(x) Y'_n(y) \tag{10}$$

To satisfy the essential boundary conditions, the modal shape functions are chosen based on the combination of boundary conditions on the four plate sides which can include simply supported, clamped, or free. Dugundji [1988] determined approximate shape functions for generalized boundary conditions and arbitrary high-order modes. These

shape functions allow for the simulation of any combination of edge boundary conditions while maintaining numerical stability for high-order modes which is required for plate transient analysis and impact. Here, a subset of these shape functions is provided for reference. Similar expressions can be determined for other combinations of boundary conditions using the approach outlined in [Dugundji, 1988]. For an FSDT plate simply supported on all four sides, Eq. (11) satisfies the necessary conditions of $w = 0$ at $\mathrm{x} = 0, \mathrm{L}_x$ and $w = 0$ at $\mathrm{y} = 0, \mathrm{L}_y$ [Reddy, 2004].

$$\begin{aligned} X_m(x) &= \sqrt{2}\sin\left(\frac{m\pi x}{L_x}\right) \\ Y_n(y) &= \sqrt{2}\sin\left(\frac{n\pi y}{L_y}\right) \end{aligned} \tag{11}$$

Fully clamped boundary conditions require that $w = \phi_x = 0$ at $\mathrm{x} = 0, \mathrm{L}_x$ and $w = \phi_y = 0$ at $\mathrm{y} = 0, \mathrm{L}_y$ [Reddy, 2004] therefore the modal shape functions in Eq. (12) are used to represent the spatially-dependent plate displacements and rotations.

$$\begin{aligned} X_m(x) &= \sqrt{2}\sin\left(\left(m+\frac{1}{2}\right)\pi\left(\frac{x}{L_x}\right)-\frac{\pi}{4}\right)+e^{-\left(m+\frac{1}{2}\right)\pi\left(\frac{x}{L_x}\right)}+(-1)^{m+1}e^{-\left(m+\frac{1}{2}\right)\pi\left(1-\frac{x}{L_x}\right)} \\ Y_n(y) &= \sqrt{2}\sin\left(\left(n+\frac{1}{2}\right)\pi\left(\frac{y}{L_y}\right)-\frac{\pi}{4}\right)+e^{-\left(n+\frac{1}{2}\right)\pi\left(\frac{y}{L_y}\right)}+(-1)^{n+1}e^{-\left(n+\frac{1}{2}\right)\pi\left(1-\frac{y}{L_y}\right)} \end{aligned} \tag{12}$$

In substituting the series approximations for the transverse displacement, planar rotations, and lateral load into the expressions for kinetic and potential energy, performing the necessary differentiation and integration, and solving Lagrange's equation of motion, one achieves three equations which can be solved for the three unknown modal amplitudes (W_{mn}, A_{mn}, and B_{mn}). The first two equations resulting from

$$-\frac{\partial L}{\partial A_{mn}} = 0 \tag{13}$$

and

$$-\frac{\partial L}{\partial B_{mn}} = 0 \tag{14}$$

can be solved simultaneously for expressions of A_{mn} and B_{mn} with respect to W_{mn}. These equations can then be substituted into the equation resulting from

$$\frac{d}{dt}\left[\frac{\partial L}{\partial \dot{W}_{mn}}\right]-\frac{\partial L}{\partial W_{mn}}=0 \tag{15}$$

to yield a single equation with respect to $\ddot{W}_{mn}$, W_{mn}, and Q_{mn}. The resulting equation can be cast in the form

$$[S]\left[\ddot{W}\right]+[T][W]=\left[\bar{Q}\right] \tag{16}$$

where $\left[\ddot{W}\right]$ and $[W]$ are matrices with components $\ddot{W}_{mn}$ and W_{mn}, respectively, and $[S]$ and $[T]$ are coefficient matrices. The force term $\left[\bar{Q}\right]$ is a function of the generalized forces $Q_{mn}(t)$ and the mode shapes as follows

$$\bar{Q}_{mn}=Q_{mn}(t)\iint_{A_c} X_m^2(x)Y_n^2(y)dA_c \tag{17}$$

The generalized forces $Q_{mn}(t)$ are computed via

$$Q_{mn}(t)=\frac{\iint_{A_c} q(x,y,t)X_m(x)Y_n(y)dA_c}{\iint_{A_c} X_m^2(x)Y_n^2(y)dA_c} \tag{18}$$

where the lateral force, $q(x,y,t)$, taken as a uniform distribution of the total contact force over the square contact area, can be expressed as

$$q(x,y,t)=\frac{F(t)}{A_c(t)} \tag{19}$$

and therefore removed from the surface integral. Here, $F(t)$ is the contact force distributed uniformly over a square area, A_c, where $A_c=\pi\left[R_s^2-\left(R_s-\alpha(t)\right)^2\right]$. R_s is the radius of the spherical indentor and α is the indentation of the plate expressed as

$$\alpha(t)=u(t)-w(\xi,\eta,t) \tag{20}$$

where $u(t)$ is the displacement of the indentor and $w(\xi,\eta,t)$ is the plate lateral displacement at the impact location.

Note that the contact area changes as a function of time-dependent plate indentation. The contact force is governed by Hertz contact law [Sun and Chen, 1985]

$$F(t)=k_H\alpha(t)^{3/2} \tag{21}$$

with the Hertzian contact stiffness expressed as [Qian and Swanson, 1990]

$$k_H=\frac{4}{3}\sqrt{R_s}E_{33} \tag{22}$$

where E_{33} is the transverse Young's modulus of the lamina. Assuming rigid-body dynamics of the impactor, Newton's 2nd law provides

$$F = -m\ddot{u}(t) \tag{23}$$

Therefore the motion of the impactor can be described via

$$\ddot{u}(t) = -\frac{k_H}{m}\left(u(t) - w(\xi,\eta,t)\right)^{3/2} \tag{24}$$

where m is the mass of the indentor.

Because of the nonlinearity of the ODE in time governing the motion of the indentor, a predictor-corrector method is employed. This involves freezing $u(t)$ and $w(\xi,\eta,t)$ to solve for $\ddot{u}(t)$, then updating $\ddot{u}(t)$ with the newly computed values of $u(t)$ and $w(\xi,\eta,t)$. The procedure is continued until a converged value of $\ddot{u}(t)$ is achieved. The coupled equations that govern the deformation of the plate and motion of the indentor (Eqs. (16) and (24), respectively) are solved numerically using the implicit Newmark β method [Newmark, 1959]. The basic equations of this method are

$$\begin{aligned} W_{t+\Delta t} &= W_t + \Delta t\dot{W}_t + \left(1/2-\beta\right)\Delta t^2\ddot{W}_t + \beta\Delta t^2\ddot{W}_{t+\Delta t} \\ \dot{W}_{t+\Delta t} &= \dot{W}_t + \left(1-\gamma\right)\Delta t\ddot{W}_t + \Delta t\gamma\ddot{W}_{t+\Delta t} \end{aligned} . \tag{25}$$

Assuming that the general form of the dynamic response of a damped system (i.e., equilibrium equation) is satisfied at time $t+\Delta t$ provides

$$A\ddot{W}_{t+\Delta t} + B\dot{W}_{t+\Delta t} + CW_{t+\Delta t} = F_{t+\Delta t} \tag{26}$$

When $B=0$ in Eq. (26), it resembles the form of Eq. (16). Therefore, the solution for Eq. (16) can be achieved by applying Newmark's β method as shown in Eq. (25). In this solution, Newmark's constant average-acceleration scheme (trapezoidal rule) with γ=1/2 and β=1/4 is employed to provide for unconditionally stable solution. The initial conditions for the numerical solution are shown in Eq. (27).

$$\begin{aligned} &W_{mn} = \dot{W}_{mn} = \ddot{W}_{mn} = 0 \\ &u = \ddot{u} = 0, \quad \dot{u} = v_0 \end{aligned} \tag{27}$$

where v_0 is the initial velocity of the impactor.

Once the series of equations is solved for W_{mn}, the lateral displacement and in-plane rotations can be computed for each time step. It is then possible to compute the various strain components in the laminate such as interlaminar shear strain [Reddy, 2004] as follows

$$\gamma_{xz} = \phi_x + w_{,x} \tag{28}$$

and

$$\gamma_{yz} = \phi_y + w_{,y} \tag{29}$$

which can then be used to compute the resultant interlaminar shear forces [Reddy, 2004], Q_x and Q_y, as seen in Eqs. (30) and (31), respectively.

$$Q_x = k\left(A_{55}\gamma_{xz} + A_{45}\gamma_{yz}\right) \tag{30}$$

$$Q_y = k\left(A_{44}\gamma_{yz} + A_{45}\gamma_{xz}\right) \tag{31}$$

The final output of the composite impact model is the displacement, strain, and stress fields over the entire plate for the duration of the impact event as well as the impactor displacement and force histories.

B. Composite Plate Damage Model

A failure model is required to determine the composite damage state from the predicted plate deformation and stresses due to impact. This model must be compatible with the previously described deformation model and maintain the desired computational efficiency. Using a single-layer theory such as FSDT precludes the use of more advanced damage or delamination modeling approaches such as those based on virtual crack closure technique (VCCT) [Krueger, 2004], cohesive zone model (CZM) [Turon et al., 2007], floating node method (FNM) [Chen et al., 2014], or extended finite element method (XFEM) [Tay et al., 2014] which require the damage to be explicitly modeled and are very computationally expensive. Furthermore, necessary simplicity of the desired modeling framework requires damage to be predicted in a post-processing sense rather than as progressive damage – therefore the presence of damage will not affect the plate kinematics. It will be demonstrated that for typical laminates and impact scenarios, sufficient accuracy is maintained through this one-way coupling damage prediction method.

Preliminary efforts by the present authors investigating the feasibility of using a purely stress-based damage criterion, such as those presented in Refs. [Dobyns, 1981; Chang and Chang, 1987; Brewer and Lagace, 1988], determined that the damage parameters were sensitive to the laminate layup. For investigations within a single material system and layup, such an approach would suffice. However, since the intended use of the developed model is to serve as a sizing tool to optimize composite laminate configurations, including layup, minimizing calibration across layups

is desired. In other words, ideally the damage model will have parameters that can be calibrated for a specific material system and used across layups. To address the deficiencies of a fully stress-based approach, an energy-based delamination propagation criterion was employed along with a stress-based damage initiation criterion. This combination allows strength to govern the initiation of damage and linear elastic fracture mechanics (LEFM) to control its propagation.

Predicting the shape, size, and location of the BVID requires the discretization of the plate into a uniform array of small elements referred to as damage cells as seen in Fig. 2. In a typical analysis, over 12,000 damage cells are used to discretize a standard 75 x 125 mm plate. The choice of damage cell size does not affect the plate kinematics (i.e., no mesh dependence) but only the resolution of predicted damage. Each cell contains the effect of all through-thickness plies comprising the laminate at that location. Provided with the plate kinematics at each time step from the composite plate deformation model, the BVID model determines whether damage is present at each discretized cell. The damage model employed for this effort is adapted from Zubillaga et al. [2014] and extended to apply to an FSDT plate subjected to impact loading.

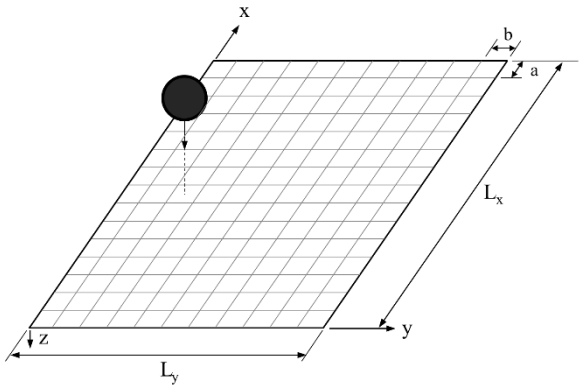

Fig. 2 Laminate discretization for damage prediction; damage cell size is a x b

The LEFM-based damage model developed by Zubillaga et al. [2014] expands on the approaches by Refs. [O'Brien, 1984; Johnson and Chang, 2001b; Maimi et al, 2011] and assumes that delamination induced by transverse matrix cracking is a major contributor to composite laminate failure [Pagano and Schoeppner, 2000]. Experimental evidence of matrix cracks triggering delaminations which lead to composite failure is provided in Refs. [Crossman and Wang, 1982; Johnson and Chang, 2001a; Hallett et al., 2008; Wisnom et al., 2008]. In González et al. [2012], transverse matrix cracks are considered initiation points for delaminations. Additionally, under low velocity impact loading, it has been shown experimentally that matrix cracks precede delamination growth and that transverse matrix

cracks serve as a precursor to delamination for BVID [Chang et al., 1990; Richardson and Wisheart, 1996; Topac et al., 2017]. The model is based on the idea that the laminate elastic strain energy released due to matrix crack induced delamination (MCID) provides the driving force for delamination propagation. The MCID model considers a laminate containing a transverse matrix crack under arbitrary loading conditions, as seen in Fig. 3. Delaminations initiate from the matrix crack boundaries along the interfaces of the cracked ply, separating the laminate into damaged (Region 2) and undamaged (Region 1 and 3) regions as shown in Fig. 3. There is also a transition zone between these regions that is not depicted in Fig. 3. As demonstrated by Zubillaga et al. [2014], the energy stored in the transition region is not a function of delamination length, s, if the cracks are sufficiently spaced. In the case of small crack spacing where the transition region stress fields interact, assuming an abrupt transition between damaged and undamaged regions (i.e., no transition region) yields a more conservative prediction of crack driving force [Zubillaga et al., 2014]. Therefore in this work, as is done in Zubillaga et al. [2014], the transition region is not considered for damage and failure prediction.

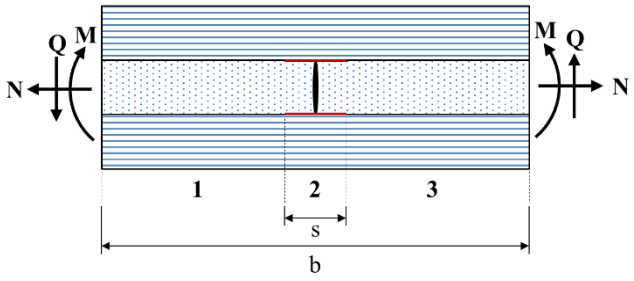

Fig. 3 Laminate damage cell cross section with matrix crack induced delamination

Since damage at each location in the plate is determined based on the strain energy available to propagate the delamination, the strain energy as a function of delamination length must be computed. Similar to how the potential energy is expressed over the entire plate in Eq. (4), the strain energy due to bending and transverse shear for a laminate can be written in integral form as

$$U = \frac{1}{2}\int_0^{L_x}\int_0^{L_y}\left\{\kappa^T D\kappa + \kappa\gamma^T A_{TS}\gamma\right\}dydx \tag{32}$$

where κ and γ are the curvature and transverse shear strain, respectively [Cairns and Lagace, 1989]. By discretizing the plate into many small damage cells of dimension a x b as illustrated in Fig. 2, the curvature and transverse shear strain can be assumed constant within each damage cell and removed from the surface integral. Since the curvature and transverse shear (κ and γ) are computed at the center of each damage cell, this assumption states that the value

at the center of the damage cell is a good approximation of the mean value across the interval. By multiplying this value by the size of the damage cell, the midpoint rule can be employed to approximate the definite integral. Therefore the integral from Eq. (32), taken over a single damage cell, can be reduced to

$$U_{dc} = \frac{ab}{2}\left(\kappa^T D\kappa + \not{\kappa}\gamma^T A_{TS}\gamma\right), \tag{33}$$

where U_{dc} is the strain energy stored in a particular damage cell of size a x b. As shown in Fig. 3, the cross-section of each damage cell can be divided into pristine and damaged regions where the damaged region contains a transverse matrix crack inducing a delamination. The contribution of the pristine (Region 1 and 3) and damaged (Region 2) regions to the strain energy is

$$U_{dc} = \frac{1}{2}a(b-s)\left(\kappa^T D\kappa + \not{\kappa}\gamma^T A_{TS}\gamma\right) + \frac{1}{2}as\left(\kappa^T D^*\kappa + \not{\kappa}\gamma^T A^*_{TS}\gamma\right), \tag{34}$$

where the first term on the right-hand side is the contribution of the pristine region and the second term is from the damaged region. D^* and A^*_{TS} are the reduced D and A_{TS} matrices for the damaged region. It can be observed that as the delamination grows, energy is transferred from the pristine to the damaged regions. Next, the strain energy release rate, G, which describes the elastic energy released per change in delamination area, is derived using the expression shown in Eq. (35).

$$G = -\frac{\partial U}{\partial A} = -\frac{\partial U}{a \cdot ds \cdot m} \tag{35}$$

where m is the number of delaminations per ply and ds is the change in delamination length. Substituting Eq. (34) into Eq. (35) yields

$$G = -\frac{1}{2m}\left(\kappa^T \bar{D}\kappa + \not{\kappa}\gamma^T \bar{A}_{TS}\gamma\right) \tag{36}$$

where $\bar{D} = D^* - D$ and $\bar{A}_{TS} = A^*_{TS} - A_{TS}$.

Determining the reduced D and A_{TS} matrices (D^* and A^*_{TS}) requires that the effect of a transverse matrix crack and corresponding interfacial delaminations on the laminate behavior be carefully considered. For this, consider a hypothetical stack of three plies (N=3) as shown in Fig. 4. In the general case, this stack would represent all the plies comprising each damage cell of the discretized laminate (Fig. 2). It is assumed for this case that a transverse matrix crack (black vertical plane) in Ply 2 has initiated delaminations (hatched horizontal planes) at both interfaces of the damage cell. To determine the effect of this damage on the laminate elastic behavior, the contribution of the matrix

crack is investigated first. The contribution of the transverse matrix crack aligned with the fibers in Ply 2 will be in the form of reduced matrix-dominated properties [Johnson and Chang, 2001b]. Therefore for the cracked ply, $E_{22} = G_{12} = \nu_{12} = 0$ while the fiber-dominated tensile modulus is unaffected (i.e., $E_{11} = E_{11}$). Using Classical Laminate Theory (CLT), the laminate bending stiffness components can be determined by summing the bending stiffnesses of the individual plies in the damage cell stack, transformed to the laminate coordinate system, via $D^* = \sum_{k=1}^{N} D_k$. While the effect of transverse crack is accounted for in the bending stiffness (D) reduction, delaminations affect the transverse shear extensional stiffnesses (A_{IS}). Due to the presence of interfacial delaminations, such as the hatched regions in Fig. 4, the damage cell stack will be unable to sustain laminate interlaminar shear loading (i.e., $G_{yz} = G_{xz} = 0$). Therefore since $A_{IS} = f(G_{yz}, G_{xz})$, the interlaminar shear stiffness, and therefore the transverse shear extensional stiffnesses, of the damage cell stack will equal zero ($A_{IS}^* = 0$).

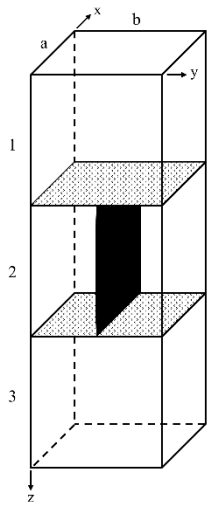

Fig. 4 Laminate damage cell stack with matrix crack induced delamination present

This procedure is repeated for every layer in the laminate stack as shown in Fig. 5. Once the reduced laminate stiffness are known for each possible MCID position through the thickness, the energy-based model can be run at each time step for every damage cell. The computed value of strain energy release rate (G) can be compared with its critical value (G_c) and once $G \geq G_c$ for at least one layer, the delamination is assumed to propagate over the extent of the damage cell.

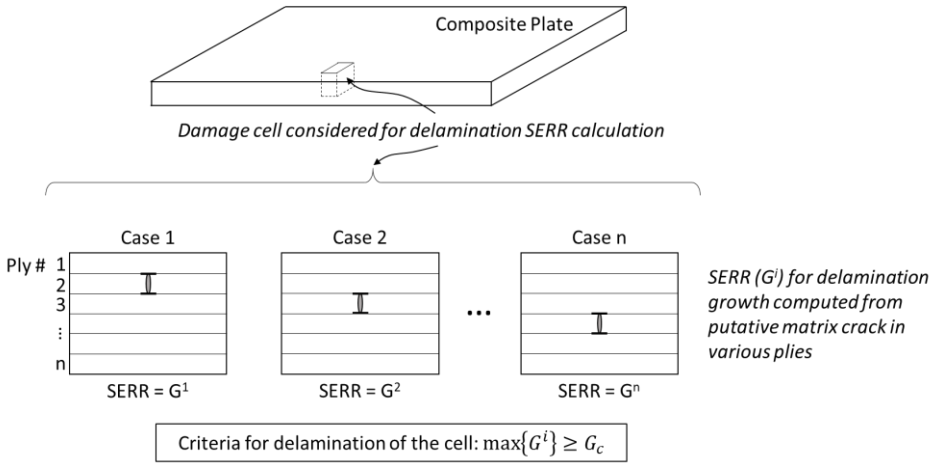

Fig. 5 Procedure to determine strain energy release rate (SERR) for each potential MCID position

The developed energy-based damage model determines whether a previously-initiated delamination will propagate and induce cell damage. In composite laminates under low velocity impact conditions, there typically exists a threshold impact velocity or energy below which no delamination will form [Choi and Chang, 1990; Schoeppner and Abrate, 2000; González et al., 2011]. In order to capture this delamination threshold, the energy-based damage propagation model is coupled with a Hashin stress-based damage initiation model [Hashin, 1980] of the form

$$\sigma_{13}^2 + \sigma_{23}^2 \geq S_{ILS}^2 \tag{37}$$

where S_{ILS} is the laminate strength for both components of interlaminar shear stress. Combining a stress-based initiation model with an energy-based growth model allows damage to be predicted over a large range of impact energies and damage sizes.

III. Results and Discussion

A large testing program over multiple fiber architectures, layups, impact velocities, and impactor masses, was conducted to validate the developed damage initiation and propagation model. Ultrasonic C-scan measurements were used to compare with the model predictions. The model accuracy was assessed against the experimental damage size and morphology.

A. Material and Experimental Impact Testing

Impact testing was performed on AS4/8552 composite plates of two fiber architectures – unidirectional (UD) tape and plain weave (PW) fabric – and three layups per architecture. The panels were manufactured and rough-cut in house and the specimens were finished and tested by the National Institute for Aviation Research (NIAR). The material properties of the AS4/8552 plies are consistent with the published data on this material system [González, 2011]. A summary of the fiber architecture/layup combinations tested is provided in Table 1. From this table, it can be observed that each architecture includes one quasi-isotropic (Layup 1), one "soft" (Layup 2), and one "hard" (Layup 3) layup. The layups referred to as "soft" or "hard" are those with fewer or more than 25% of the plies in the 0° orientation, respectively. At least three different impact velocities were tested for each architecture/layup combination, ranging from 123.7 to 445.6 cm/s (48.69 to 175.4 in/s). A hemispherical tup impactor with a diameter of 1.5875 cm (0.625 in) and mass of either 2.7 or 6.1 kg (5.96 or 13.45 lb_m) were used for the impact tests. The various combinations of laminates, impact velocities, and impactor masses provided a wide range of damage from no damage to an area of 9.33 cm^2 (1.45 in^2). The impact tests were performed following the procedure prescribed in ASTM D7136 [ASTM D7136, 2015], including using a plate size of 100 x 150 mm (4" x 6") and the standard test fixture. In total, 54 impact tests were performed. Output from these tests included the load and impactor displacement histories. Following each test, through-thickness ultrasonic C-scan measurements were performed to determine the damage morphology and size.

Table 1 Summary of composite impact test fiber architectures and layups

	Unidirectional (UD) tape	**Plain weave (PW) fabric**
Layup 1	$[45/0/-45/90]_{4s}$	$[45/0/-45/90]_{3s}$
Layup 2	$[45/-45/0/45/-45/90/45/-45/45/-45]_{2s}$	$[45/-45/0/45/-45/45/-45/90/45/-45]_{s}$
Layup 3	$[45/0/90/0/-45/0/45/0/-45/0]_{2s}$	$[0/90/45/0/90/0/90/-45/0/90]_{s}$

B. Impact Damage Model Results and Validation

The impact damage prediction model described in Section II was called upon to simulate the impact event and predict the resulting damage for all 54 cases tested. For each case, the test was replicated using the model including details of the prescribed fiber architecture, layup, and impact parameters. To validate the accuracy of the plate deformation model, the predicted contact force history is compared with the experiment. A typical force history output is shown in Fig. 6 for two different sets of boundary conditions, simply supported and clamped on all four sides which can be abbreviated as SSSS and CCCC, respectively. As previously described, the model was developed to be fully

general in terms of boundary conditions; therefore any combination of simply supported, clamped, and free edge supports can be investigated. It is evident from the contact force history in Fig. 6 that the SSSS boundary condition most closely represents what is experienced during the ASTM D7136 test. This finding is in agreement with Refs. [Fuoss et al., 1998; González et al., 2011; Abir et al., 2017]. Using the fully simply supported boundary conditions, the model predicted the first half of the curve well indicating that the global plate deformation and boundary conditions are being simulated correctly. Near the peak of the contact force history, the curves begin to diverge due to the formation of damage. As mentioned, the developed damage model only contains one-way coupling (kinematics → damage). Therefore the damage that is predicted to form during the load history does not have an impact on the contact force or plate deformation. An assessment of the model's ability to predict impact damage size will be presented showing this simplifying assumption does not introduce appreciable error into the model.

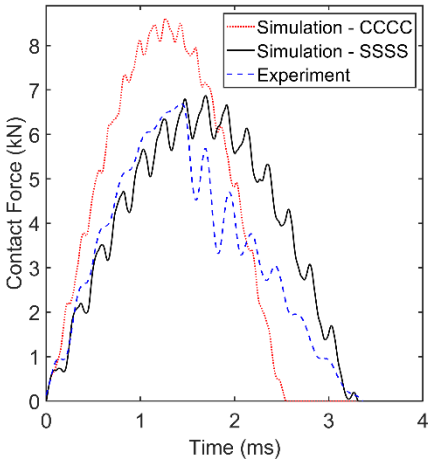

Fig. 6 Contact force history prediction

After verifying that the model was capable of accurately modeling the plate transient deformation, simulations were performed to predict the composite damage for each of the 54 cases. The damage model runs for the uniform grid of damage cells as shown in Fig. 2 and produces a two dimensional (2D) profile of the resulting damage. The output is similar to the data obtained from a through-thickness C-scan since it provides a 2D profile of the damage without details of the damage position through the thickness. For preliminary design and analysis, this type of damage information is sufficient for comparison to experimental data and for computing plate residual strength. A comparison of the model results and C-scan data for the damaged UD cases is shown in Fig. 7. The model plate is shown in blue with yellow damaged cells overlaid on the C-scan images. The black region in the middle of the C-scan image is the experimental damage while the other black regions are the clamps and calibration markers. The white text overlaid on

the images includes the specimen ID and impact velocity. The specimen ID includes the fiber architecture (UD in this case), layup (L1, L2, L3) and the specimen number. It can be observed that the modeled plate is smaller than the experimental plate because the exposed, unsupported region of the plate of size 75 x 125 mm (3" x 5") is simulated in the model.

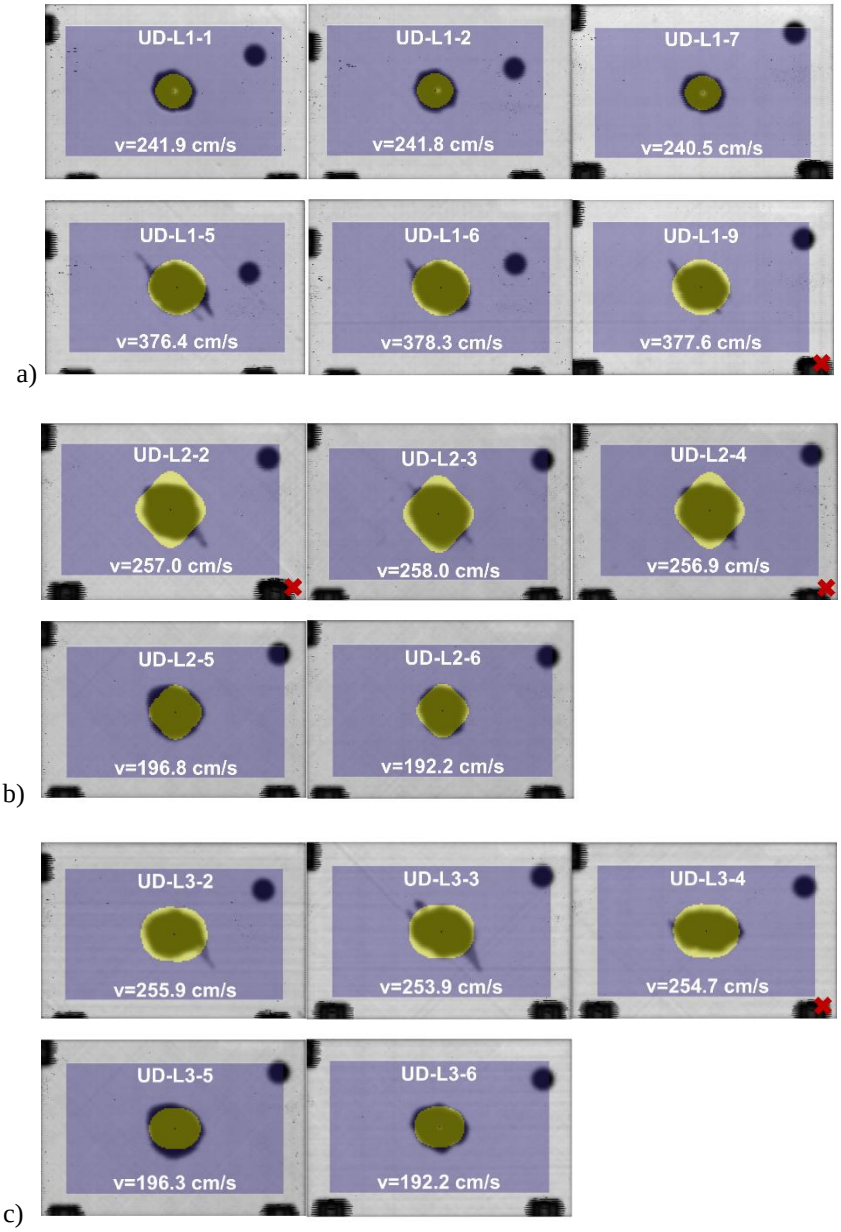

Fig. 7 Unidirectional laminate impact damage prediction for a) Layup 1; b) Layup 2; c) Layup 3

Comparisons between the size and shape of the predicted and measured damage in Fig. 7 demonstrate the ability of the model to accurately simulate impact damage over multiple layups and impactor velocities of the same UD fiber architecture. The only calibration required for the damage model involves determining the critical strain energy release

rate, G_c. Since the LEFM-based model predicts the total strain energy release rate (G) based on the energy released in the laminate due to a propagating MCID, there is no information available regarding the relative magnitudes of its individual components. Because of this lack of mode-mixity information, traditional delamination propagation criteria which compare the individual components of G to their corresponding critical values cannot be used. Therefore the value of G_c is calibrated for a single case to match the experimental results. It was determined that a value between G_{Ic} and G_{IIc} fits the experimental data well. For the UD and PW damage models, calibrated values of 391.4 J/m^2 (2.235 psi*in) and 1290 J/m^2 (7.365 psi*in) were used. Bounding the calibrated value of G_c by G_{Ic} and G_{IIc} indicates that the total G predicted by the model contains a mixture of G_I and G_{II} which can be calibrated from a single impact test on one laminate configuration (quasi-isotropic, in the present case). This greatly simplifies calibration. Importantly, it was determined that G_c is independent of layup, indicating that its value can be calibrated for one layup and used for any other layup of the same material system with similar ply thicknesses.

Besides the qualitative assessment presented in Fig. 7, the damage area predictions were compared with the experimental results as shown in Fig. 8 where A_{exp} is the experimental damage area measured via C-scan and A_{sim} is the simulated damage area taken as the pixel area of the damage grid. In this figure, the blue dashed line indicates a perfect prediction while the red dotted lines provide the 30% error bounds. It can be observed that the model accurately predicts the impact damage area for most of the UD cases. Specifically, an error of 30% or less is maintained for 75% (12/16) of the damage cases with a mean error of 23.23%. This magnitude of error is typically acceptable for a modeling tool used for preliminary design and analysis. The cases that exceed the 30% error bounds are highlighted with a red “x” in the lower-right corner of the test image in Fig. 7. For some of the cases where the damage was overpredicted, additional failure modes, such as fiber splitting, can be observed in the experimental C-scans, such as for UD-L1-9 and UD-L2-2. Since the only energy dissipative mechanism considered in the model is delamination propagation, it is not surprising that the model overpredicts the damage in these cases.

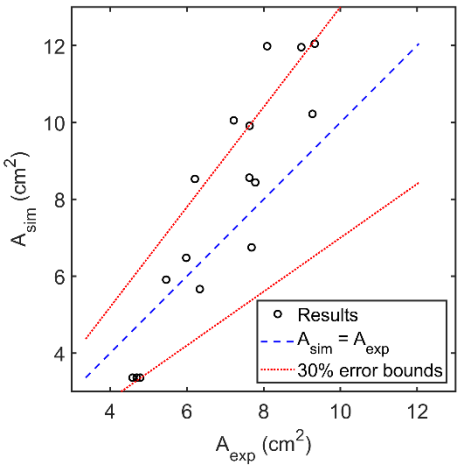

Fig. 8 Model damage prediction compared with experimental results for unidirectional laminate

For the cases where impact resulted in damage as observed in the C-scan results, the model has been shown capable of accurately predicting BVID shape and size. However, the energy-based model cannot predict the threshold behavior, i.e., it cannot predict an abrupt drop to zero damage below a certain impact velocity. This behavior has been observed experimentally in Refs. [Choi and Chang, 1990; Schoeppner and Abrate, 2000; González et al., 2011]. The threshold impact velocity represents the initiation of rapid delamination formation and growth and is typically associated with the peak impact force and subsequent load drop [Zhang, 1998] (see also the experimental curve in Fig. 6). This initiation of delamination at the threshold velocity is typically followed by stable delamination growth [Jackson and Poe, 1993], which the present energy-based damage model, as discussed in the foregoing, is able to predict. As a comprehensive impact damage prediction tool must also predict the threshold behavior, we combine the energy-based model with the strength-based model to determine the conditions where the transition from no delamination to finite delamination (as predicted by the energy model) occurs. The threshold behavior is typically represented as a plot of damage size versus impact velocity [Choi and Chang, 1992]. However, as the threshold velocity is a function of the plate dimension, boundary conditions, and layup, we cast the threshold phenomena in terms of a threshold damage size which represents the minimum delamination area required to serve as a pre-crack for the energy-based model. This threshold damage size is calibrated using the strength model (Eq. (37)) in conjunction with experimental threshold data for one laminate geometry (plate size, boundary condition) and layup. The threshold damage size is determined by modeling impact tests over a range of velocities and matching the predicted threshold damage velocity to the experiments using the strength-based model. At a minimum, at least one impact case resulting

in delamination and one without delamination is required to determine the threshold velocity. Calibrating the threshold damage size for the UD and PW laminates gives the values of 0.435 and 0.629 cm^2, respectively.

Once the threshold damage size is calibrated, the overall impact damage prediction workflow is as follows: the strength-based model is used to predict the delamination size which is compared with the threshold damage size; if the predicted damage size is less that the threshold damage size, the delamination area is set to zero. Once the delamination size predicted by the strength model exceeds the threshold damage size, the energy-based damage model is used to predict the delamination size. As an illustration, this workflow is applied to the UD Layup 1 to predict the delamination size as a function of impact velocity. In Fig. 9a, the output of the stress-based model is shown. The intersection between the delamination area prediction and the experimentally determined threshold damage size determines the threshold velocity. The output of the combined (stress + energy based models) presented in Fig. 9b shows the overall predicted response. It is seen that the combined strength-based and energy-based model is able to capture the threshold behavior and is qualitatively consistent with the experimental data where no damage was seen until a velocity of 222.3 cm/s, followed by a monotonic increase in delamination area with impact velocity. It may also be noted from Fig. 9 that the stress-based model significantly under predicts the delamination area for impact velocities greater than the threshold velocity. On the other hand, as discussed earlier (see Fig. 8), the delamination area predicted by the energy-based model is in good agreement with the experimental data.

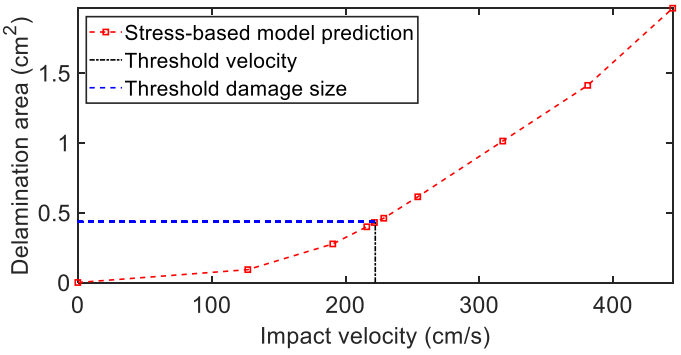

a)

b)

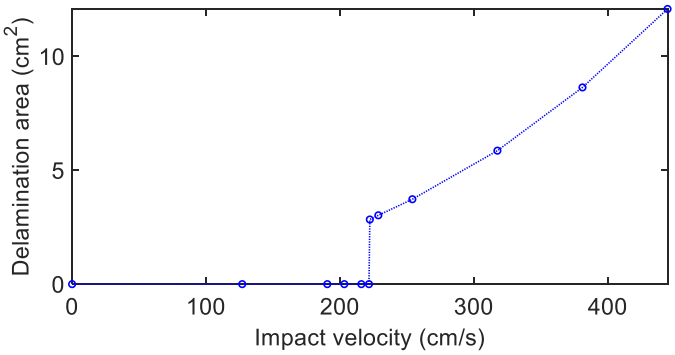

Fig. 9 Model output over a range of velocities demonstrating a) the stress-based model prediction of damage threshold velocity and b) the overall model prediction of damage threshold and delamination propagation

Once the damage model was fully calibrated for initiation in addition to propagation, validation over all UD test cases (27 in total) was conducted. This included all the cases presented in Fig. 7 and Fig. 8 as well as 11 cases where no damage existed following impact. The validation plot for all 27 cases is shown in Fig. 10 and a summary is provided in Table 2. Nine out of the 11 "no damage" cases are correctly predicted and overlap at the plot origin in Fig. 10. Two of the "no damage" cases, however, were predicted to have damage. Since the damage initiation model acts as a switch, if the model predicts the presence of damage incorrectly, the error will be large, as seen in the two points at $A_{\text{exp}} = 0$ that exceed the 30% error bounds. Fortunately this error is on the side of conservatism (i.e., predicting damage when there is none). Out of the 27 UD cases, the damage area was predicted within 30% for 21 cases and the mean error was 14.87%.

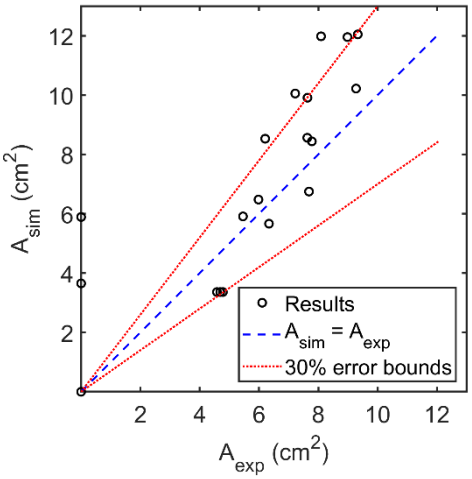

Fig. 10 Unidirectional laminate impact damage results summary including "no damage" cases

Table 2 Summary of unidirectional composite impact tests and simulation results

Specimen	Velocity (cm/s)	Mass (kg)	Damage area (cm^2)	Model area (cm^2)	Error
UD-L1-1	241.9	2.703	4.781	3.361	-29.69%
UD-L1-2	241.8	2.703	4.690	3.361	-28.34%
UD-L1-3	134.5	2.703	0.000	0.000	0.00%
UD-L1-4	133.5	2.703	0.000	0.000	0.00%
UD-L1-5	376.4	2.703	7.781	8.439	8.46%
UD-L1-6	378.3	2.703	7.626	8.561	12.27%
UD-L1-7	240.5	2.703	4.581	3.361	-26.62%
UD-L1-8	194.9	2.703	0.000	0.000	0.00%
UD-L1-9	377.6	2.703	6.206	8.529	37.42%
UD-L2-1	219.4	2.703	0.000	3.652	INF
UD-L2-2	257.0	6.101	8.090	11.981	48.09%
UD-L2-3	258.0	6.101	9.329	12.045	29.11%
UD-L2-4	256.9	6.101	8.981	11.955	33.12%
UD-L2-5	196.8	6.101	7.684	6.748	-12.17%
UD-L2-6	192.2	6.101	5.981	6.477	8.31%
UD-L2-7	136.0	6.101	0.000	0.000	0.00%
UD-L2-8	133.0	6.101	0.000	0.000	0.00%
UD-L2-9	133.4	6.101	0.000	0.000	0.00%
UD-L3-1	289.5	2.703	0.000	5.890	INF
UD-L3-2	255.9	6.101	9.271	10.219	10.23%
UD-L3-3	253.9	6.101	7.632	9.910	29.84%
UD-L3-4	254.7	6.101	7.219	10.052	39.23%
UD-L3-5	196.3	6.101	5.458	5.910	8.27%
UD-L3-6	192.2	6.101	6.335	5.665	-10.59%

UD-L3-7	123.7	6.101	0.000	0.000	0.00%
UD-L3-8	127.7	6.101	0.000	0.000	0.00%
UD-L3-9	126.9	6.101	0.000	0.000	0.00%

Similar to the UD impact cases, simulations were performed to replicate the tests performed on the PW specimens. Again, 27 tests were conducted for at least three velocities per layup. Comparison between the model and test damage profiles are shown in Fig. 11. In this series of tests, only one case (PW-L1-1) resulted in no damage. Evident from the overlaid damage plots in Fig. 11, the model is again proven capable of predicting the damage size and shape accurately. A quantitative comparison between measured and predicted damage area is shown in Fig. 12. It can be observed that a large majority of the predictions fall within the 30% error bounds. In fact, 78% of the cases (21/27) are predicted with less than 30% error with a mean error of 21.08%. Again, red "x" marks indicate the cases that exceed the 30% error bound in Fig. 11.

It is also evident from Fig. 12 that there is a clustering of points near the lower 30% error bound corresponding to the lower velocity cases where the model is consistently underpredicting the damage area. Noting that the impactor cross-sectional area, annotated in Fig. 12, falls within this cluster of points, it is likely that the damage observed in the ultrasonic C-scan images is superficial and includes mostly surface ply damage. Since the model does not include intraply damage, it is not surprising that the area of the predicted damage, in the form of delamination, is smaller than what is seen experimentally.

a)

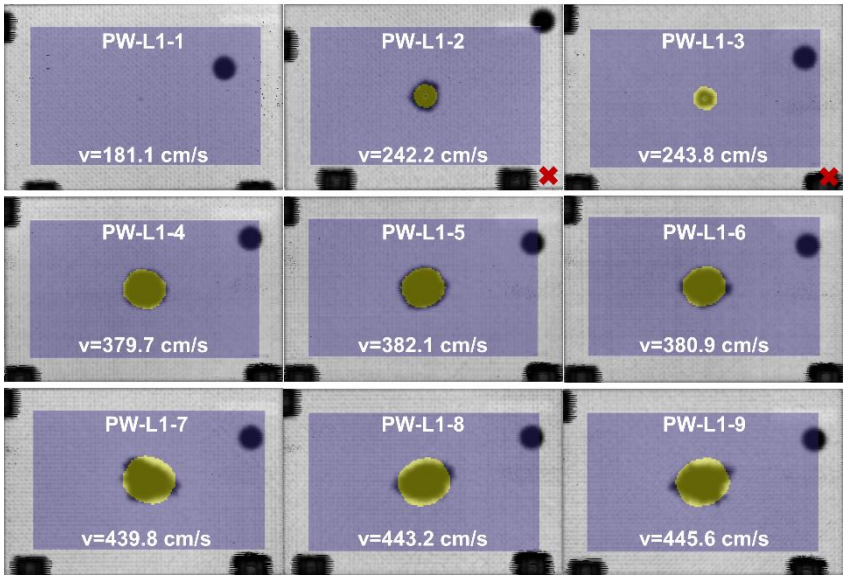

b)

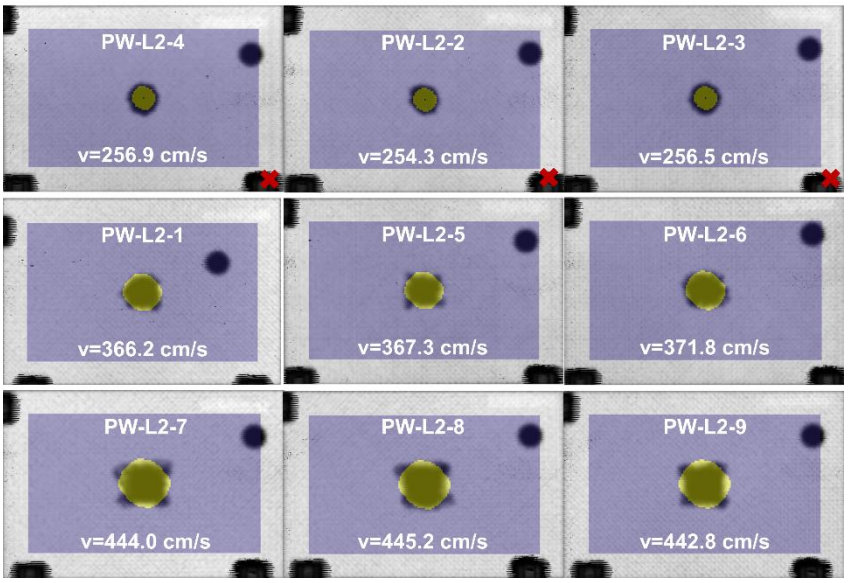

c)

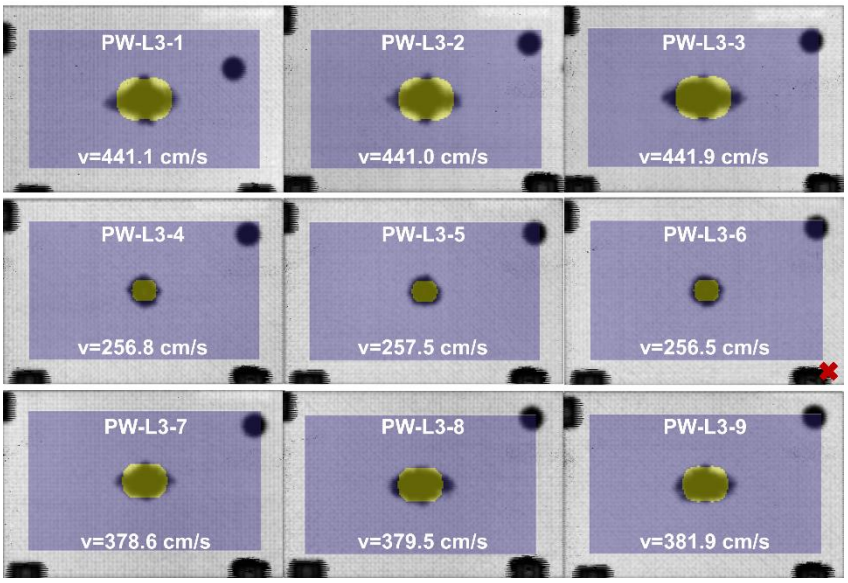

Fig. 11 Plain weave laminate impact damage prediction for a) Layup 1; b) Layup 2; c) Layup 3

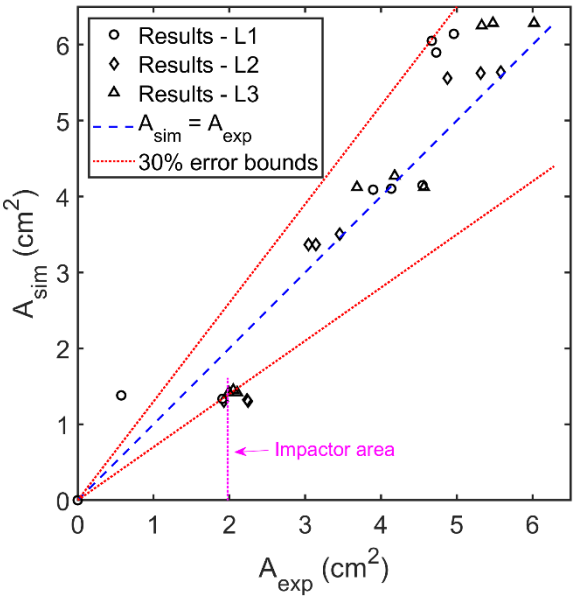

Fig. 12 Plain weave laminate impact damage results summary including "no damage" cases and highlighting individual laminate data

One source of challenge associated with the development of a rapid tool for composite impact damage prediction is the simplifying assumptions that are required to maintain efficiency and applicability to preliminary design and analysis. One such assumption involves simplifying the damage behavior, as described in Section IIB, to be dominated by MCID. Also required is a simplified calibration process. In order for such a tool to have application in preliminary design and analysis, calibration should involve fitting the fewest possible parameters to the test data and these parameters should be applicable across a range of laminates and test conditions. As was mentioned in Section IIB, a purely stress-based failure criterion was found to lack the generality required. Specifically, the primary calibration parameter, laminate ILS strength factor, was found to be dependent on the laminate layup which would severely limit the utility of the tool for rapid design. For example, calibrating the laminate ILS strength factor to the UD-L1-1 impact case from Table 2 and predicting the BVID area for all the UD-L2 and UD-L3 cases yields average absolute errors of 47% and 34%, respectively. Therefore it is clear that across layups, a fully stress-based approach is not ideal. In contrast, as seen in the validation results for the UD and PW laminates, the energy-based approach provides the necessary generality to accurately predict damage morphology and size over a wide range of layups, impactor masses, and impact velocities. To further investigate the sensitivity of the primary calibration parameter for the energy-based model, G_c, different marker styles are used in Fig. 12 for each of the three layups. From this plot it can be observed

that similar accuracy is maintain across all three layup configurations. This indicates that the calibration of the impact damage model is insensitive to layup and can be applied to the optimization of layup configurations. Finally, a detailed summary of the PW results are presented in Table 3.

Table 3 Summary of plain weave composite impact tests and simulation results

Specimen	Velocity (cm/s)	Mass (kg)	Damage area (cm^2)	Model area (cm^2)	Error
PW-L1-1	181.1	2.703	0.000	0.000	0.00%
PW-L1-2	242.2	2.703	1.910	1.335	-30.07%
PW-L1-3	243.8	2.703	0.574	1.381	140.45%
PW-L1-4	379.7	2.703	3.897	4.090	4.97%
PW-L1-5	382.1	2.703	4.548	4.148	-8.79%
PW-L1-6	380.9	2.703	4.135	4.103	-0.78%
PW-L1-7	439.8	2.703	4.729	5.897	24.69%
PW-L1-8	443.2	2.703	4.671	6.052	29.56%
PW-L1-9	445.6	2.703	4.961	6.142	23.80%
PW-L2-1	366.2	2.703	3.045	3.368	10.59%
PW-L2-2	254.3	2.703	1.929	1.303	-32.44%
PW-L2-3	256.5	2.703	2.245	1.303	-41.95%
PW-L2-4	256.9	2.703	2.232	1.323	-40.75%
PW-L2-5	367.3	2.703	3.142	3.368	7.19%
PW-L2-6	371.8	2.703	3.458	3.503	1.31%
PW-L2-7	444.0	2.703	5.316	5.626	5.83%
PW-L2-8	445.2	2.703	5.581	5.639	1.04%
PW-L2-9	442.8	2.703	4.877	5.561	14.02%
PW-L3-1	441.1	2.703	5.477	6.284	14.72%
PW-L3-2	441.0	2.703	5.329	6.252	17.31%
PW-L3-3	441.9	2.703	6.019	6.284	4.39%
PW-L3-4	256.8	2.703	1.994	1.419	-28.80%
PW-L3-5	257.5	2.703	2.052	1.452	-29.25%
PW-L3-6	256.5	2.703	2.103	1.419	-32.52%
PW-L3-7	378.6	2.703	3.684	4.123	11.91%
PW-L3-8	379.5	2.703	4.568	4.123	-9.75%
PW-L3-9	381.9	2.703	4.181	4.271	2.16%

IV. Conclusion

Preliminary design and analysis of composite structures requires access to efficient BVID models. Because of the significant reduction in residual strength of these materials when impacted [Maio et al., 2013], impact resistance and CAI strength are key design parameters. As such, in order to minimize the number of expensive tests required to design and optimize composite structures, a rapid BVID prediction tool was developed and validated against

experimental impact data. The model is based the Rayleigh-Ritz method applied to a Mindlin-Reissner plate with arbitrary boundary conditions and subjected to an impact event. Damage is simulated as MCID using a strength-based initiation model and an LEFM-based propagation model. The mechanics-based modeling approach was chosen over more common FEA-based models in order to maintain the necessary efficiency for initial design and optimization; the developed model has a runtime of minutes rather than hours for a comparable FEA model. An extensive experimental program was conducted consisting of 54 total tests over multiple fiber architectures, layups, impact velocities, and impactor masses. Each of the 54 tests were simulated and the predicted damage size compared to C-scan measurements. Validation included not only predicting the damage area, but also the damage threshold. It was shown that the developed model provides accurate predictions of damage size (error less than 30% for over 75% of cases) and runs in less than two minutes. Based on its demonstrated accuracy and efficiency, the developed BVID model can effectively serve as an integral part of a comprehensive BVID/CAI strength rapid analysis framework [Borkowski and Kumar, 2018a].

Funding Sources

The material is based upon work supported by NASA under Award Nos. NNL09AA00A and 80LARC17C0004. Any opinions, findings, and conclusions or recommendations expressed in this material are those of the author(s) and do not necessarily reflect the views of the National Aeronautics and Space Administration.

References

Abir, M. R., Tay, T. E., Ridha, M., & Lee, H. P. (2017). Modelling damage growth in composites subjected to impact and compression after impact. *Composite Structures*, *168*, 13-25.

Abrate, S. (2005). *Impact on composite structures*. Cambridge university press.

ASTM D7136 / D7136M-15. (2015). Standard Test Method for Measuring the Damage Resistance of a Fiber-Reinforced Polymer Matrix Composite to a Drop-Weight Impact Event, ASTM International, West Conshohocken, PA, 2015, www.astm.org

Birman, V., & Bert, C. W. (1987). Behaviour of laminated plates subjected to conventional blast. *International Journal of Impact Engineering*, *6*(3), 145-155.

Borkowski, L., & Kumar, R. S. (2018a). Rapid Analysis Method for Composite Compression after Impact Strength Prediction. In *2018 AIAA/ASCE/AHS/ASC Structures, Structural Dynamics, and Materials Conference* (p. 0484).

Borkowski, L., & Kumar, R. S. (2018b). Inverse method for estimation of composite kink-band toughness from open-hole compression strength data. *Composite Structures*, *186*, 183-192.

Brewer, J. C., & Lagace, P. A. (1988). Quadratic stress criterion for initiation of delamination. *Journal of composite materials*, *22*(12), 1141-1155.

Cairns, D. S., & Lagace, P. A. (1989). Transient response of graphite/epoxy and kevlar/epoxy laminates subjected to impact. *AIAA journal*, *27*(11), 1590-1596.

Chang, F. K., & Chang, K. Y. (1987). A progressive damage model for laminated composites containing stress concentrations. *Journal of composite materials*, *21*(9), 834-855.

Chang, F. K., Choi, H. Y., & Jeng, S. T. (1990). Study on impact damage in laminated composites. *Mechanics of Materials*, *10*(1-2), 83-95.

Chen, B. Y., Pinho, S. T., De Carvalho, N. V., Baiz, P. M., & Tay, T. E. (2014). A floating node method for the modelling of discontinuities in composites. *Engineering Fracture Mechanics*, *127*, 104-134.

Choi, H. Y., & Chang, F. K. (1990). Impact Damage Threshold of Laminated Composites,". *Failure Criteria and Analysis in Dynamic Response", ASME, Applied Mechanics Division*, 31-35.

Choi, H. Y., & Chang, F. K. (1992). A model for predicting damage in graphite/epoxy laminated composites resulting from low-velocity point impact. *Journal of composite materials*, *26*(14), 2134-2169.

Crossman, F. W., & Wang, A. (1982). The dependence of transverse cracking and delamination on ply thickness in graphite/epoxy laminates. In *Damage in Composite Materials: Basic Mechanisms, Accumulation, Tolerance, and Characterization*. ASTM International.

Dobyns, A. L., & Porter, T. R. (1981). A study of the structural integrity of graphite composite structure subjected to low velocity impact. *Polymer Engineering & Science*, *21*(8), 493-498.

Dobyns, A. L. (1981). Analysis of simply-supported orthotropic plates subject to static and dynamic loads. *AIAA Journal*, *19*(5), 642-650.

Dugundji, J. (1988). Simple expressions for higher vibration modes of uniform Euler beams. *AIAA journal*, *26*(8), 1013-1014.

Fuoss, E., Straznicky, P. V., & Poon, C. (1998). Effects of stacking sequence on the impact resistance in composite laminates. Part 2: prediction method. *Composite Structures*, *41*(2), 177-186.

González, E. V., Maimí, P., Camanho, P. P., Lopes, C. S., & Blanco, N. (2011). Effects of ply clustering in laminated composite plates under low-velocity impact loading. *Composites Science and Technology*, *71*(6), 805-817.

González, E. V., Maimí, P., Camanho, P. P., Turon, A., & Mayugo, J. A. (2012). Simulation of drop-weight impact and compression after impact tests on composite laminates. *Composite Structures*, *94*(11), 3364-3378.

Hallett, S. R., Jiang, W. G., Khan, B., & Wisnom, M. R. (2008). Modelling the interaction between matrix cracks and delamination damage in scaled quasi-isotropic specimens. *Composites Science and Technology*, *68*(1), 80-89.

Hashin, Z. (1980). Failure criteria for unidirectional fiber composites. *Journal of applied mechanics*, *47*(2), 329-334.

Hou, J. P., Petrinic, N., Ruiz, C., & Hallett, S. R. (2000). Prediction of impact damage in composite plates. *Composites Science and Technology*, *60*(2), 273-281.

Jackson, W. C., & Poe, C. C. (1993). The use of impact force as a scale parameter for the impact response of composite laminates. *Journal of Composites, Technology and Research*, *15*(4), 282-289.

Johnson, P., & Chang, F. K. (2001a). Characterization of matrix crack-induced laminate failure—Part I: Experiments. *Journal of composite materials*, *35*(22), 2009-2035.

Johnson, P., & Chang, F. K. (2001b). Characterization of Matrix Crack-Induced Laminate Failure—Part II: Analysis and Verifications. *Journal of composite materials*, *35*(22), 2037-2074.

Krueger, R. (2004). Virtual crack closure technique: history, approach, and applications. *Applied Mechanics Reviews*, *57*(2), 109-143.

Maimı, P., Camanho, P. P., Mayugo, J. A., & Turon, A. (2011). Matrix cracking and delamination in laminated composites. Part I: Ply constitutive law, first ply failure and onset of delamination. *Mechanics of materials*, *43*(4), 169-185.

Maio, L., Monaco, E., Ricci, F., & Lecce, L. (2013). Simulation of low velocity impact on composite laminates with progressive failure analysis. *Composite Structures*, *103*, 75-85.

Mindlin, R. D. (1951). Influence of rotatory inertia and shear on flexural motions of isotropic, elastic plates. *J. Appl. Mech.*, *18*, 31-38.

Newmark, N. M. (1959). A method of computation for structural dynamics. *Journal of the engineering mechanics division*, *85*(3), 67-94.

O'Brien, T. K. (1985). Analysis of local delaminations and their influence on composite laminate behavior. In *Delamination and debonding of materials*. ASTM International.

Pagano, N. J., & Schoeppner, G. A. (2000). Delamination of polymer matrix composites: problems and assessment, pp. 433-528.

Qian, Y., & Swanson, S. R. (1990). A comparison of solution techniques for impact response of composite plates. *Composite Structures*, *14*(3), 177-192.

Reddy, J. N. (2004). *Mechanics of laminated composite plates and shells: theory and analysis*. CRC press.

Reissner, E. (1945). The effect of transverse shear deformation on the bending of elastic plates. *J. appl. Mech.*, A69-A77.

Schoeppner, G. A., & Abrate, S. (2000). Delamination threshold loads for low velocity impact on composite laminates. *Composites Part A: applied science and manufacturing*, *31*(9), 903-915.

Sun, C. T., & Chattopadhyay, S. (1975). Dynamic response of anisotropic laminated plates under initial stress to impact of a mass. *Journal of applied mechanics*, *42*(3), 693-698.

Sun, C. T., & Chen, J. K. (1985). On the impact of initially stressed composite laminates. *Journal of Composite Materials*, *19*(6), 490-504.

Tay, T. E., Sun, X. S., & Tan, V. B. C. (2014). Recent efforts toward modeling interactions of matrix cracks and delaminations: an integrated XFEM-CE approach. *Advanced Composite Materials*, *23*(5-6), 391-408.

Timoshenko, S. P., & Woinowsky-Krieger, S. (1959). *Theory of plates and shells*. McGraw-Hill.

Turon, A., Davila, C. G., Camanho, P. P., & Costa, J. (2007). An engineering solution for mesh size effects in the simulation of delamination using cohesive zone models. *Engineering fracture mechanics*, *74*(10), 1665-1682.

Whitney, J. M., & Nuismer, R. J. (1974). Stress fracture criteria for laminated composites containing stress concentrations. Journal of composite materials, 8(3), 253-265.

Whitney, J. M., & Pagano, N. J. (1970). Shear deformation in heterogeneous anisotropic plates. *Journal of applied mechanics*, *37*(4), 1031-1036.

Wisnom, M. R., Khan, B., & Hallett, S. R. (2008). Size effects in unnotched tensile strength of unidirectional and quasi-isotropic carbon/epoxy composites. *Composite Structures*, *84*(1), 21-28.

Zhang, X. (1998). Impact damage in composite aircraft structures-experimental testing and numerical simulation. Proceedings of the Institution of Mechanical Engineers, Part G: *Journal of Aerospace Engineering*, *212*(4), 245-259.

Zubillaga, L., Turon, A., Maimí, P., Costa, J., Mahdi, S., & Linde, P. (2014). An energy based failure criterion for matrix crack induced delamination in laminated composite structures. *Composite Structures*, *112*, 339-344.